The Astrophysical Journal, 961:21 (13pp), 2024 January 20 https://doi.org/10.3847/1538-4357/ad0cb6

A Numerical Study of the Effects of a Corotating Interaction Region on Cosmic-Ray Transport. II. Features of Cosmic-Ray Composition and Rigidity

Xi Luo[1], Marius S. Potgieter[1,2], Ming Zhang[3], and Fang Shen[4]
[1] Shandong Institute of Advanced Technology (SDIAT), 250100 Jinan, Shandong, People's Republic of China; xi.luo@iat.cn
[2] Institute for Experimental and Applied Physics (IEAP), Christian-Albrechts University in Kiel, D-24118 Kiel, Germany
[3] Department of Physics and Space Sciences, Florida Institute of Technology, Melbourne, FL 32901, USA
[4] SIGMA Weather Group, State Key Laboratory of Space Weather, National Space Science Center, Chinese Academy of Sciences, Beijing 100190, People's Republic of China
Received 2023 May 26; revised 2023 October 16; accepted 2023 November 13; published 2024 January 11

Abstract

We continue the numerical modeling of a corotating interaction region (CIR) and the effects it has on solar-rotational recurrent variations of galactic cosmic rays (GCRs). A magnetohydrodynamic model is adapted to simulate the background solar wind plasma with a CIR structure in the inner heliosphere, which is incorporated into a comprehensive Parker-type transport model. The focus is on the simulation of the effects of a CIR on GCR protons and the two helium isotopes as a function of heliolongitude. This is to establish whether the difference in composition affects how they are modulated by the CIR in terms of their distribution in longitude. It is demonstrated that particle diffusion and drift influence the effects of the CIR with increasing rigidity from 100 MV up to 15 GV. It is found that protons and helium isotopes are modulated differently with longitude by the CIR and that particle drift influences the modulation effects in longitude. These differences dissipate with increasing rigidity. The final results are focused on the simulated amplitude of these GCR flux variations as a function of rigidity. The amplitude displays a power-law behavior above ∼1 GV with an index similar to the power index of the rigidity dependence of the assumed diffusion coefficients. The simulations further show that below this rigidity, the amplitude at first flattens off, displaying a plateau-like profile, but it then increases systematically with decreasing rigidity below ∼0.3 GV. Again, a power-law behavior is displayed, but it is completely different from that above 1 GV.

Unified Astronomy Thesaurus concepts: Galactic cosmic rays (567); Heliosphere (711); Solar activity (1475); Solar wind (1534)

1. Introduction

Corotating interaction regions (CIRs) are long-lasting, relatively large-scale plasma structures generated in low- and medium-latitude regions of the inner heliosphere. They are the manifestation of the interactions of fast solar wind streams with the slow solar wind. These high-speed streams, originating from coronal holes, are corotating while flowing radially outward, and when they overtake the surrounding slower-speed solar wind, they also create forward and reverse shocks along the CIR. For a recent review, see Richardson (2018). These CIRs may merge as they propagate outward to form corotating merge interaction regions (CMIRs), and the related compression and rarefaction regions cause successive increases and decreases in galactic cosmic rays (GCRs). Based on multiple observations (Richardson 2004), it follows that transient CIRs (or CMIRs) cause local variations in the GCR flux, but they do not seem to significantly change the global distribution of GCRs in the heliosphere. However, the modulation efficiency of CIRs over longer timescales (solar cycles) is not established, and it is simply assumed that the total modulation effect of CMIRs over timescales of the periodic 11 yr cycle is relatively small (see the assessment made by Heber et al. 1999 and recent views on this aspect by Krainev et al. 2023).

Periodic variations in the GCR intensity measured at an observational point such as at the Earth on a timescale of 27 days are well known, as recently emphasized by Modzelewska et al. (2020). These effects on GCRs are especially prominent during the declining phase of the solar cycle, but not exclusively so, depending on solar activity conditions applicable to GCRs at different phases of the solar cycle. They usually seem to occur at low heliolatitudes, where the heliospheric magnetic field (HMF) has a well-established sector structure and coronal holes spread to lower heliolatitudes. These conditions usually prevail at and near times of solar cycle minima. The characteristic 27 day variation in GCRs is thus mostly evident during the minimum and near-minimum epochs of solar activity and may last over relatively long periods, even up to about one year, as recently reported by Aguilar et al. (2021). Their strength evidently varies with rigidity over time (solar activity). They are also observed by ground-based neutron monitors (NMs; e.g., Gil & Alania 2016), at high heliolatitudes by Ulysses (Kunow et al. 1995; Heber et al. 1999), and even beyond 60 au by Voyager 1 (Decker et al. 1999; see the reviews by Gazis et al. 1999; Kunow et al. 1999; McKibben et al. 1999). Of particular interest is how the value of the maximum decrease of these GCR variations depends on rigidity, which is usually reported as the "amplitude of the 27 day variation," as done by Modzelewska et al. (2020).

Concerning numerical modeling of the CIR characteristics, simulations have been done over the years, at first using simplified magnetohydrodynamic (MHD) models

(Jokipii & Kóta 1995; Kóta & Jokipii 1991). Good progress has been made with combined MHD and modulation models (so-called hybrid models; e.g., Guo & Florinski 2016). It has remained a challenge to numerically model CIRs based on advancements in MHD simulations and to make convincing conclusions about their effects of GCRs. Uncertainties exist, and further numerical modeling and a subsequent comparison with observational data seem needed to improve and restrain the relevant modeling parameters (Kopp et al. 2017). These uncertainties also pertain to what is to be used as solar modulation parameters and entities in numerical modulation models, and at which level of sophistication and difficulty this is possible to do. For recent advances in MHD modeling in this context and how it relates to GCR transport, see Ghanbar & Florinski (2023). The common purpose of all the numerical modeling studies is to contribute meaningfully to advancing our understanding of this interesting heliospheric phenomenon.

Part I of our study (Luo et al. 2020, hereafter Part I) was dedicated to performing a numerical study of the effects of a CIR on GCR transport as well as possible. This was based on the MHD model of Shen et al. (2018), which simulates the solar wind plasma profile for the period of Carrington rotation 2066. We used a stochastic differential equation (SDE) method to build a hybrid GCR transport model to produce the basic features of the effects of a CIR on GCR transport. Subsequently, we carried out investigations into how the CIR affects GCRs at different heliocentric radial distances and heliolatitude and how GCRs of different energies respond to the simulated CIR. We continue our modeling efforts by focusing on the simulation of the effect of a CIR on GCR protons and the two GCR helium isotopes, specifically in terms of their distribution in heliolongitude. We aim to establish whether this difference in composition affects how they are modulated by the CIR with longitude. It is demonstrated that particle diffusion and drift influence these effects with increasing rigidity from 100 MV up to 15 GV. The final and main results are focused on the simulated amplitude of the CIR-induced GCR variation as a function of rigidity.

2. Hybrid Numerical Model for GCR Transport

In this section, the essence of the hybrid numerical model is briefly discussed because the modeling approach has been described in detail in Part I.

2.1. Heliospheric Transport Background with a CIR

The interplanetary solar wind plasma is usually treated as an MHD flow, and the characteristics are described by MHD equations. Pizzo (1982) modeled a CIR based on three-dimensional (3D) single-fluid MHD equations and studied how the magnetic field affects the evolution process of the CIR in the inner heliosphere. Later, in order to meet challenges in space weather, a comprehensive MHD numerical model (ENLIL) was developed that was able to simulate coronal mass ejections, CIRs, and other solar wind structures (Odstrcil 2003). For recent advances in MHD modeling of these inner heliospheric structures, see also Shiota et al. (2017) and Usmanov et al. (2018). Developing dedicated MHD numerical models for studying CIR effects on GCR transport followed, e.g., by Guo & Florinski (2014), Wiengarten et al. (2014), Kopp et al. (2017), and Ghanbar & Florinski (2023).

It remains a challenge to model GCR transport and their modulation in interplanetary plasma with CIRs based on MHD and SDE simulations. Taking this type of modeling to the level that comparison with observational data is meaningful is not easily done, although it is important and a continuous objective to restrain relevant transport parameters. Shen et al. (2018) made such an attempt. Driven by the synoptic magnetogram maps, the inner boundary condition of the MHD model is assigned with fewer free parameters. Correspondingly, the simulated solar wind parameters from 2007 to 2017 capture the general time pattern of the observational data. This improved MHD model was adapted and used in Part I as well as in this study.

The MHD model is applied up to 27 au, and an extrapolated Parker magnetic field is employed beyond. While the plasma background boundary in Luo et al. (2020) is set at 80 au, we include a simplified MHD shock model for the termination shock (TS) located at 92 au. Using a grid system, the first grid point is at 0.19 au, which is also the inner boundary, whereas the outermost grid point is at 145.52 au, but the outer modulation boundary is manually set at 130 au. Following the MHD Rankine–Hugoniot relation, the solar wind and magnetic field across the TS vary according to the following equations:

$$\begin{aligned} \boldsymbol{V}_{\rm sw} &= V_{r0}(1/C_r)\left(\frac{r_{ts}}{r}\right)^2 \hat{e}_r, \\ b_r &= b_{r0}\left(\frac{r_{\rm in}}{r}\right)^2 C_r, \\ b_\theta &= b_{\theta 0}\left(\frac{r_{\rm in}}{r_{\rm ts}}\right) C_r\left(\frac{r}{r_{\rm ts}}\right), \\ b_\phi &= b_{\phi 0}\left(\frac{r_{\rm in}}{r_{\rm ts}}\right) C_r\left(\frac{r}{r_{\rm ts}}\right). \end{aligned} \tag{1}$$

Here, $\boldsymbol{V}_{r0}$, b_{r0}, $b_{\theta 0}$, and $b_{\phi 0}$ are the solar wind radial component and the IMF radial, polar, and azimuthal components upstream of the TS; C_r is the TS shock-compression ratio, which is set at 3.3, and $r_{\rm ts} = 92$ au is the radial distance location of the TS.

The solar wind plasma flow is treated as an incompressible plasma fluid, thus $\nabla \cdot \boldsymbol{V}_{\rm sw} = 0$. Due to the shock compression, the magnetic field increases beyond the TS. Similar to our previous GCR study (Luo et al. 2011), the magnetic field components b_r decreases with $\frac{1}{r^2}$, and b_θ and b_ϕ increase with radius r, which is different from the Parker magnetic field in the heliosheath. To recapitulate, the MHD simulation of the CIR is done for $r \leqslant 27$ au; for 27 au $< r \leqslant 92$ au, the solar wind expansion is assumed to be radial with a constant velocity; and for 92 au $< r \leqslant 130$ au, the solar wind and HMF behaved according to Equation (1). The full simulation domain is thus a sphere with a heliocentric radius of 130 au.

Figure 1 shows the plasma background profile in the heliospheric equatorial (XY) plane, with the Sun located at the center. This profile is used as input for the GCR transport model. The different colors illustrate the magnitude of the solar wind velocity, whereas the solid line with arrows indicates the interplanetary magnetic field direction. The change in color in the inner heliosphere indicates the presence of a CIR, and the blue region represents a slower solar wind velocity beyond the TS. For an enlarged view of

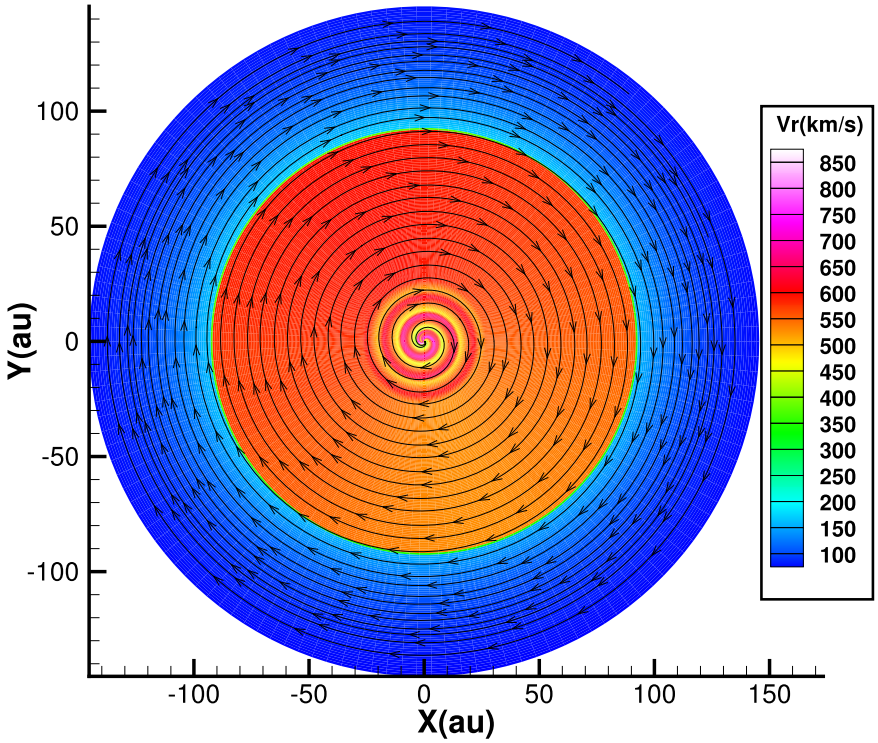

Figure 1. The plasma background profile in the heliospheric equatorial (XY) plane, with the Sun located at the center, used as input for the GCR transport model. The different colors illustrate the magnitude of the solar wind velocity, whereas the solid line with arrows denotes the interplanetary magnetic field direction. The change in color in the inner heliosphere indicates the presence of a CIR, and the blue region represents a slower solar wind velocity beyond the the TS up to the heliopause. Note that the modulation boundary is manually set at 130 au. For an enlarged view of the CIR structure in the inner heliosphere, see Figure 1 in Part I, and also additional illustrations by Krainev et al. (2023).

the simulated CIR structure in the inner parts of the heliosphere, see Figure 1 in Part I. Additional discussion and illustrations of this modeling are given by Krainev et al. (2023).

2.2. Monte Carlo and Hybrid GCR Transport Model

Our GCR transport numerical model is based on the Parker transport equation (PTE; Parker 1965),

$$\frac{\partial f}{\partial t} = -(\boldsymbol{V}_{\rm sw} + \boldsymbol{V}_d)\cdot\nabla f + \nabla\cdot(\boldsymbol{K}_s\cdot\nabla f) + \frac{1}{3}(\nabla\cdot\boldsymbol{V}_{\rm sw})\frac{\partial f}{\partial \ln p}, \quad (2)$$

where the $\boldsymbol{V}_{\rm sw}$ and $\boldsymbol{V}_d$ are the solar wind speed and the particle drift speed, respectively (additionally, see Jokipii et al. 1977; Kóta & Jokipii 1983). Here, $\boldsymbol{K}_s$ is the diffusion tensor expressed in the local magnetic field coordinate system, which has the following form:

$$\boldsymbol{K}_s = \kappa_\perp I + (\kappa_\parallel - \kappa_\perp)\hat{b}\hat{b}. \quad (3)$$

We use a simplified approach of assuming that $\kappa_\perp = \kappa_{\perp r} = \kappa_{\perp\theta}$.

Similar to our previous studies (Luo et al. 2011, 2013, 2015, 2016, 2020), the PTE has been converted into the following SDEs (Zhang 1999):

$$d\boldsymbol{X} = (\nabla\cdot\boldsymbol{K}_s - \boldsymbol{V}_{\rm sw} - \boldsymbol{V}_d)ds + \sum_\sigma \vec{\alpha_\sigma} dW_\sigma(s)\,, \quad (4)$$

$$dp = \frac{1}{3}p(\nabla\cdot\boldsymbol{V}_{\rm sw})ds. \quad (5)$$

These equations define the stochastic trajectories of the pseudo-particles in the phase space $(\boldsymbol{X}, p)$ with a given increment $d\boldsymbol{X}$, dp. By recording the boundary value $f_b(\boldsymbol{X}_b, p)$ at $(\boldsymbol{X}_b, p)$ where the pseudo-particle stochastic trajectory hits the outer boundary for the first time, the solution for the PTE (Equation (2)) can be obtained with the following ensemble average: $f(\boldsymbol{X}, p) = \langle f_b(\boldsymbol{X}_b, p)\rangle$. In each increment, the MHD-simulated solar wind speed and magnetic field are loaded to calculate the essential three terms of the SDE, i.e., $\boldsymbol{K}_s$, $\boldsymbol{V}_d$, and $\boldsymbol{V}_{\rm sw}$ which can correspondingly be expressed as a function of $\boldsymbol{B}$ or $V_{\rm sw}$.

The MHD simulation is carried out in the solar corotating frame, while the SDE-based GCR Monte Carlo transport model is in the inertial rest reference. Correspondingly, to propagate the GCR pseudo-particles in the corotating frame, an additional corotational velocity needs to be added in the SDE equation (see Luo et al. 2020). For details of the SDE approach, such as how the wavy HCS is handled, see Luo et al. (2013, 2017). As for the diffusion coefficients (DCs), we note that progress has been made for various diffusion theories, e.g., Zhao et al. (2017, 2018), but concerning the complexity of turbulence models and the uncertainty of its intrinsic parameters, a pragmatic phenomenological approach is adopted. For an advanced approach of how to relate the DCs to turbulence quantities associated with CIRs, see, e.g., Ghanbar & Florinski (2023). Following our previous model of the DCs, the components $K_\parallel$ and $K_\perp$ in $\boldsymbol{K}_s$ are given by the following

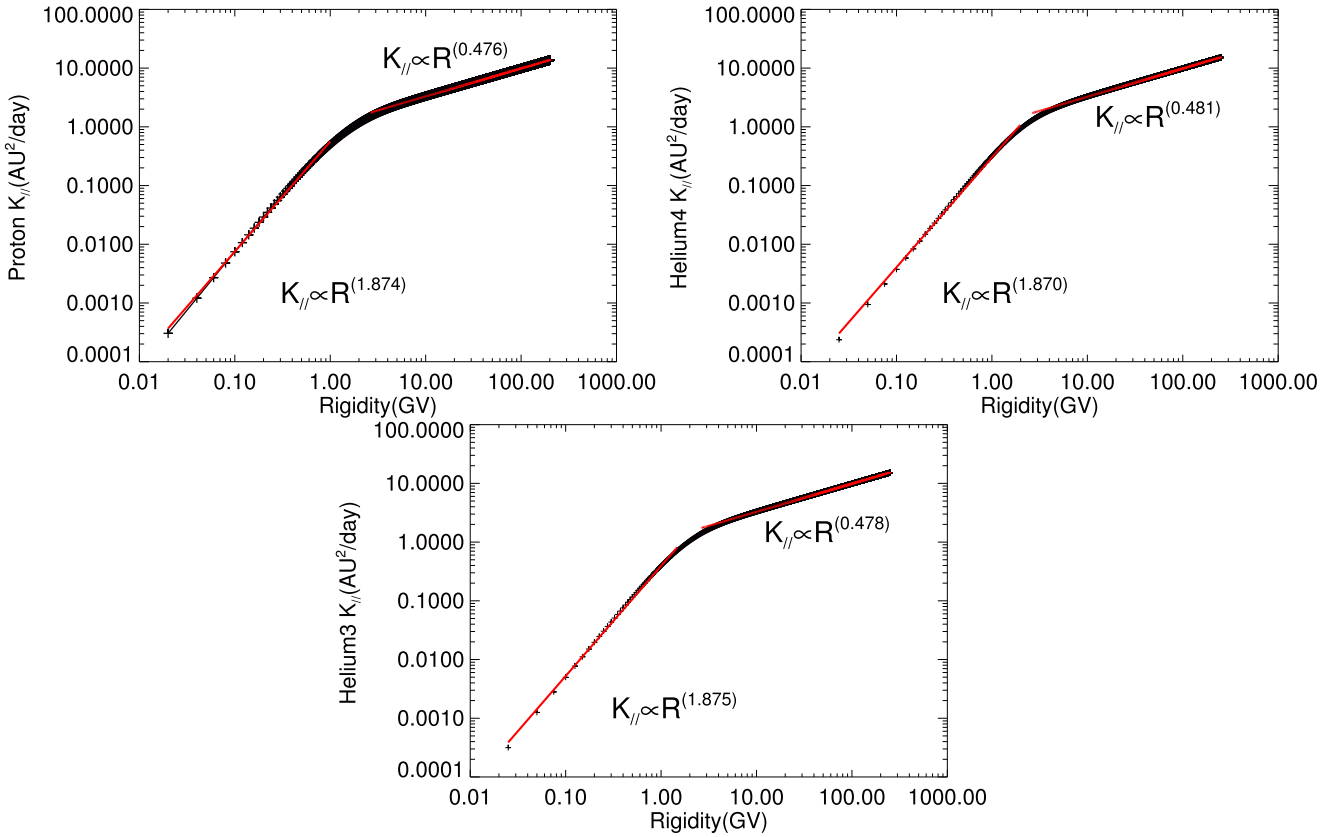

Figure 2. Rigidity dependence of the DCs according to Equations (6) and (7) for GCR protons (upper left panel), He-4 (upper right panel), and He-3 (lower panel). A double power law is assumed as the red lines indicate; for example, for protons $K_{\parallel}$ it is proportional to $R^{0.476}$ ($R^{1.874}$) in the higher (lower) rigidity range, with the change typically occurring between 2 to 4 GV.

equations:

$$K_{\parallel} = K_0 \beta \left(\frac{B_{eq}}{B}\right)\left(\frac{R}{R_0}\right)^a \left(\frac{\left(\frac{R}{R_0}\right)^c + \left(\frac{R_k}{R_0}\right)^c}{1 + \left(\frac{R_k}{R_0}\right)^c}\right)^{\frac{b-a}{c}}, \quad (6)$$

and

$$K_{\perp} = 0.02 K_{\parallel}. \quad (7)$$

Here, K_0 is a constant with the value of 17.7×10^{20} cm^2 s^{-1}, and β is the ratio of the particle speed to the speed of light; B is the interplanetary magnetic field magnitude, and B_{eq} is the interplanetary magnetic field magnitude at coordinates (1 au, 90°.0 and 0°.0) as the location of the Earth; $R_0 = 1$ GV so that the right side of the first equation is dimensionless except for the first parameter K_0. Our assumptions in this context are mostly based on reports by Potgieter et al. (2014), Ngobeni et al. (2020), Aslam et al. (2021), and Song et al. (2021). Following our previous numerical study of GCR protons and helium (He) using AMS observations (Song et al. 2021), the DC parameters are set as $R_k = 2.63$GV, $a = 0.99$, $b = 0.47$, and $c = 3.0$. This form defines a double power-law relation for the rigidity dependence of the DCs. Parameter a (b) defines the power-law index for a rigidity R lower (higher) than R_k, and c is a parameter that constrains the transition smoothness at around $R = R_k$. Note that the values of the DCs depend on the value of β. In practice, this means that for a given rigidity, e.g., 0.3 GV as we use here, the β value for protons is higher than the β value for He-4. Figure 2 displays the corresponding rigidity dependence of the DCs used in the model for GCR protons, He-4 and He-3. As it demonstrates, their rigidity dependence follows the double power-law form, with different power index values depending on the GCR species.

The pitch-angle-averaged drift velocity for an isotropic distribution is

$$\langle \vec{v_D} \rangle = (K_d)_0 \frac{pv}{3q} \nabla \times \left(\frac{\boldsymbol{B}}{B^2}\right) = (K_d)_0 \frac{\beta R}{3} \nabla \times \left(\frac{\boldsymbol{B}}{B^2}\right), \quad (8)$$

with q the charge of particles, p the particle momentum, and R the rigidity (see Forman et al. 1974; Jokipii et al. 1977 for an original theoretical description of this drift velocity). Since a turbulent magnetic field suppresses the effectiveness of the GCR particle drift (Forman et al. 1974; Engelbrecht et al. 2017; Zhao et al. 2017), here, the parameter $(K_d)_0$ is used to reduce the drift speed over the full rigidity range in order to illustrate the effect of the CIR in a straightforward manner. This means that the maximum particle drift is obtained when weak scattering is assumed with $(K_d)_0$; when, e.g., $(K_d)_0 = 0.1$, this means that the drift is reduced by a factor of 10 over the entire rigidity range. However, a more subtle reduction is found (Potgieter et al. 2014; Ngobeni & Potgieter 2015; Aslam et al. 2021) to depend on rigidity, but only below 1 GV, where it becomes significant, given by $(K_d)_0 = 10R^2/(1 + 10R^2)$. The essence of this latter process is that particle drift is not reduced at higher rigidity (see Figure 8 by Potgieter et al. 2014 and Figure 11 by Aslam et al. 2023). In the SDE model, the

heliospheric current sheet is implemented as was done by Luo et al. (2013, 2017).

The very local interstellar spectra (LISs) for GCR protons, He-3, and He-4 are specified as the outer boundary spectral values in our modulation model. They are set according to Bisschoff et al. (2019) and Ngobeni et al. (2020). For protons, this is

$$J_p(E) = 2620.0\frac{1}{\beta^2}\left(\frac{E}{E_0}\right)^{1.1}\left(\frac{(E/E_0)^{0.98} + 0.7^{0.98}}{1 + 0.7^{0.98}}\right)^{-4.0} + 30.0\frac{E}{E_0}^{2}\left(\frac{E/E_0 + 8.0}{9.0}\right)^{-12.0}, \quad (9)$$

where E is the kinetic energy (in GeV nuc^{-1}), $E_0 =$ 1 GeV nuc^{-1}, and J_p is the GCR differential intensity, with $J_p \propto p^2 f$. As for helium, the total helium intensity $J_{\rm He} = J_{\rm He3} + J_{\rm He4}$ is given as

$$J_{\rm He}(E) = 163.4\frac{1}{\beta^2}\left(\frac{E}{E_0}\right)^{1.1}\left(\frac{(E/E_0)^{0.97} + 0.58^{0.97}}{1 + 0.58^{0.97}}\right)^{-4.0}. \quad (10)$$

It is demonstrated by Ngobeni et al. (2020, 2022) that because the very LIS and the mass-charge ratios are different for He-3 and He-4, to correctly model the intensity ratio of protons to that of these He isotopes, the LISs for He-3 and He-4 need to be applied individually, with a subsequent calculation of the modulated total He. We also follow his approach.

3. Results and Discussion

In the following sections, representative simulations are displayed to illustrate the effects of the simulated CIR on the flux of GCRs.

3.1. CIR Effects on the Transport of Protons and Helium Isotopes

First, we focus on the longitudinal dependence of the simulated effects on GCRs.

3.1.1. Longitude Variation

Coronal holes are usually considered to be long-lived, so that the resulting CIRs persist for several Carrington rotations (CRs). During one CR, the CIR can be considered to be in a steady state so that we simulate the GCR flux variation with heliolongitude to reflect the effect of a CIR on GCR transport. Alternatively, the longitude variation of the GCR flux reflects how the GCR flux at some fixed location varies with time during one CR period.

In our simulation, the CIRs have already fully developed at 1 au (the Earth orbit). With increasing radial distance, one distinct CIR is well established at around 3 au (see Figures 4 and 5 by Luo et al. 2020). Because the results at 3 au are not qualitatively different from those at 1 au, the study here is restricted to 3 au. Figure 3 illustrates the flux variations of protons, He-3, and He-4 at 3 au with longitude inside a typical CIR event. The plasma background characteristics, such as the solar wind speed ($V_{\rm sw}$), the magnetic field magnitude (B), and the plasma density (N), are plotted as a function of longitude in the upper panels ((A), (B), and (C)). The longitudinal variation of the respective fluxes is demonstrated in the lower three panels ((D), (E), and (F)). In this figure, to be consistent with the observed plasma characteristic time variation near the Earth, the longitude is reverted, e.g., $\phi = 360° - \phi$. Thus, at the beginning of the CR, the Earth is located at 0° longitude and then gradually changes to 360°, coinciding with the end of this CR period (see also Yang et al. 2018). According to the simulated plasma characteristics, at around 180° heliolongitude, the magnetic field magnitude and plasma density reach a peak value, indicating that the solar wind plasma is compressed between fast and slow solar wind streams. This is highlighted with a shaded range, which indicates the simulated CIR as it follows from the MHD model. It is illustrated by panels (D), (E), and (F) that inside the CIR, the three GCR fluxes, for protons, He-3, and He-4, experience a significant depression. This scenario is consistent with the current understanding of how the CIR effects GCR transport (Richardson 2018). Additionally, the GCR flux variation demonstrates an anticorrelation with the change in solar wind speed and the associated sharp increase in the magnitude of the magnetic field. As the speed decreases from $\phi = 0°$ to $\phi = 170°$, and the associated magnetic field increases, all three GCR fluxes gradually increase. Inside the CIR, the speed and the magnetic field have sharp transitional increases with which the GCR flux depression coincides. Beyond the CIR, around $190° < \phi < 240°$, as the magnetic field decreases sharply and the solar wind speed decreases gradually, the GCR flux rises gradually. At $\phi = 270°$, there is a diminishing effect, which is not our focus in this study. These simulations evidently contribute to the view that changes in the solar wind flow with the associated changes in the magnetic field are responsible for the effects of the CIR on GCRs (Richardson 1996). The recent observational study by Dumbović et al. (2022) indicates that the maximum GCR depression (or count dip amplitude, as they call it) correlates with the peak in the magnetic field and flow speed of the CIR.

Our simulation demonstrates that protons and helium isotopic fluxes are affected by a CIR in a steady state and that they therefore become observable as a rotational recurrent effect at a given location over time. Indeed, as the AMS-02 observational data illustrate, the proton and total helium flux exhibit these 27 day variations (Aguilar et al. 2021, 2022). Our simulation also shows these types of features therefore demonstrate that the CIR is the main driver for these solar rotational recurrent variations in GCRs.

3.1.2. Ratios of Proton and Helium Isotopic Fluxes

In this section, we focus on how protons and helium isotopes respond to the simulated CIR. The PAMELA and AMS-02 experiments have provided precise measurements of the GCR flux composition over a wide range of rigidity (Adriani et al. 2013; Martucci et al. 2018; Marcelli et al. 2020; Aguilar et al. 2021, 2022). These data sets provide an opportunity to study how the flux ratios between different GCR isotopes vary with solar activity, yielding insightful understanding of the solar modulation process. Motivated by these observations, we focus on how the simulated proton and helium flux ratios are affected by a CIR in what follows. Comparisons with these extensive set of GCR observations will be made in the future.

Figure 4 shows that the proton, He-3, and He-4 fluxes vary with longitude at 3 au in the three upper panels ((A), (B), and (C)). Additionally, in the lower four panels ((D), (E), (F), and (G)), the flux ratios of protons to He-3, protons to He-4, He-4

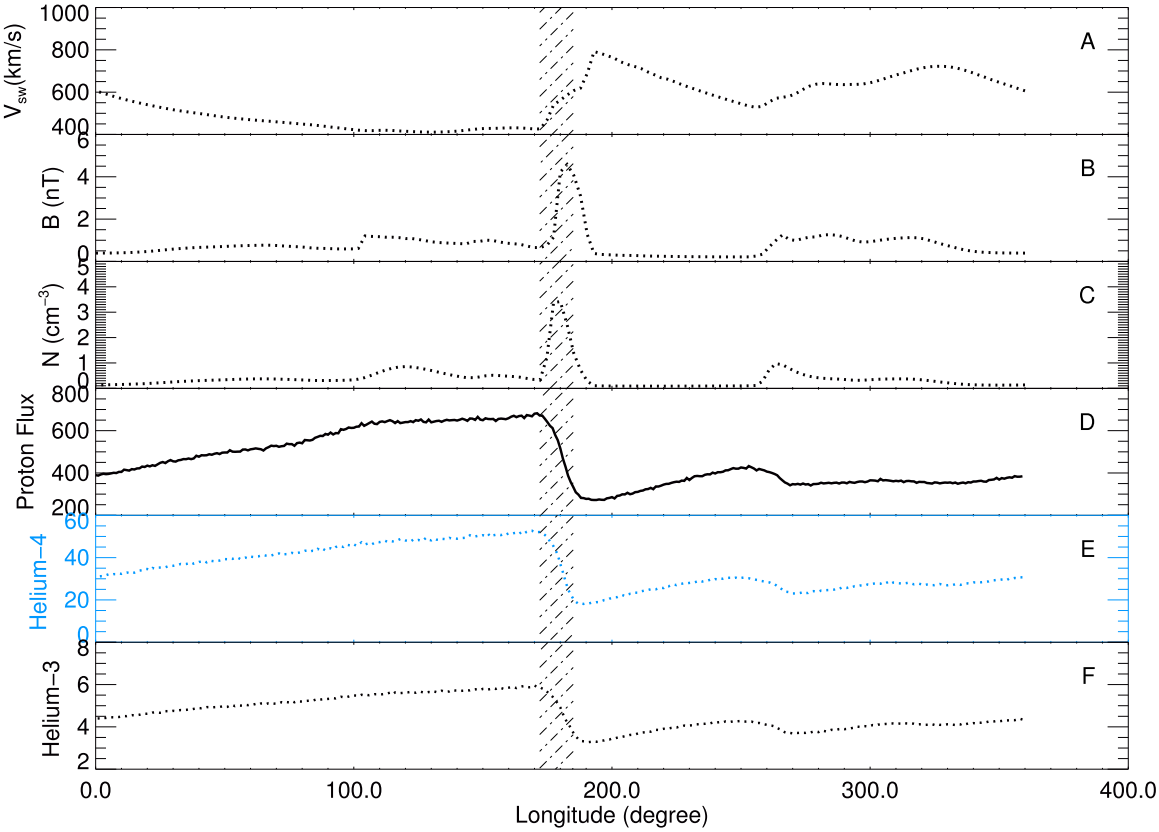

Figure 3. The plasma background characteristics, solar wind speed (V_{sw}), magnetic field magnitude (B), and plasma density (N) plotted as a function of heliolongitude in the upper panels ((A), (B), and (C)) together with the simulated 0.3 GV flux for protons, He-3, and He-4 at 3.01 au in the lower panels ((D), (E), and (F)). The units for the GCR flux are $1/(m^2/sr/s/(GeV/n))$. The shaded range indicates where the solar wind plasma is compressed between the fast and slow streams.

to He-3, and protons to total helium (He-3 plus He-4) are shown, respectively. Panel (E) shows that p/He-4 increases inside the CIR, exhibiting a peaked structure that is also evident in panel (G) for p/(total He). This indicates that at this rigidity, the change in flux caused by the CIR is weaker for protons than for He-4.

Panel (F) illustrates that the longitudinal variation of He-4/He-3 is different from the simulations in panels (E) and (G), here displaying no peaked values. Instead, the ratio decreases, followed by a significant rise in values. This behavior suggests that inside the CIR, the He-4 flux is more depressed than He-3, implying that the CIR has a stronger effect on He-4 than on He-3. The same behavior is evident from panel D, indicating that protons at this rigidity inside the CIR are more affected than He-3. These simulations indicate that the effect of the CIR is strongest for He-4, weaker for helium-3 and protons, but stronger for protons than for He-3 at this rigidity.

Figure 5 shows the results for 1.7 GV instead of 0.3 GV, as done in Figure 4. The effects at this rigidity are qualitatively similar, but are noticeable weaker than at 0.3 GV.

Concerning the proton to helium flux ratios, it is important to take note of their global modulation and the spectral intensity levels in the inner heliosphere. Ngobeni et al. (2020) studied their global modulation and found that the intensity ratio of p/He at different rigidity regimes is affected differently in the modulation processes. At a lower rigidity $R < 0.6$ GV, it becomes an interplay of both diffusion and drift with the adiabatic energy-loss process in the inner heliosphere (see their illustrative Figures 10 and 11). It follows that the modulated proton, He-4, and He-3 spectra at the Earth show peak intensities at different rigidities, which therefore relates to the peak intensities in their individual LISs and directly affects the p/He at a given position in the heliosphere as a function of rigidity.

3.2. Physical Processes and CIR Effects

It is rare that numerical modeling studies address the reasons that GCRs of different composition respond differently to the presence of a CIR. In what follows, we strive to address these aspects and issues. It seems justified to use a comprehensive SDE transport model with a solar wind plasma background based on MHD modeling. We consider that both the diffusion and drift processes play a role in how GCRs are transported, and therefore, also play a role inside a CIR. In terms of global modulation, it is reported by Zhang (1997) that a linear relation exists between the latitude gradient of the GCR intensity in the heliosphere and the amplitude of the 27-day recurrent variation in GCRs. This implies that the mechanisms influencing the latitudinal gradient should also have an effect on the 27 day variation. It should be noted that later studies using data from the Ulysses and PAMELA experiments for a different period did not confirm this linear relation (Dunzlaff et al. 2008; de Simone et al. 2011). For the modeling of global GCR gradients, see, e.g., Vos & Potgieter (2016) and Shen et al. (2021), and for an update on observational latitudinal gradients, see Gieseler & Heber (2016).

Although it has long been known that particle drift plays a substantial role in global GCR propagation (Jokipii et al. 1977; Kóta & Jokipii 1983; Potgieter & Moraal 1985), its role inside a CIR is rarely addressed and has not been properly quantified.

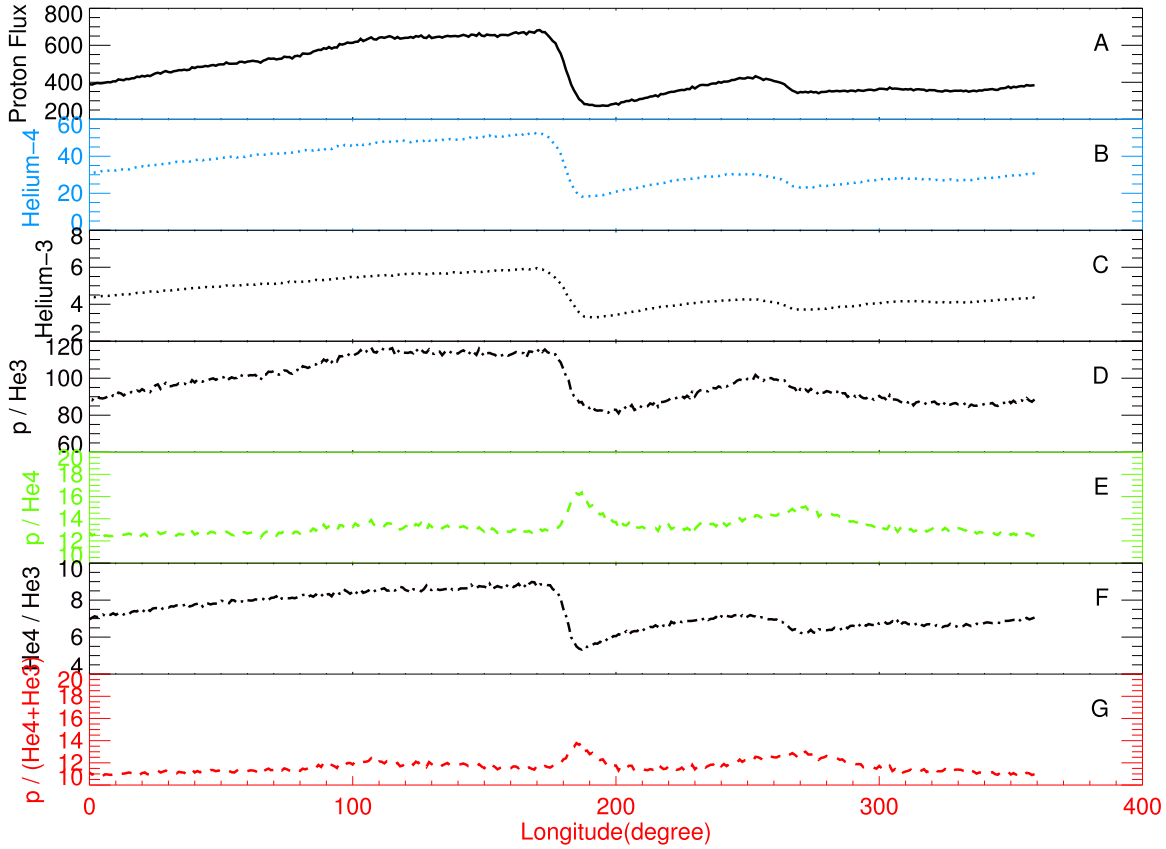

Figure 4. Simulated 0.3 GV proton flux and helium isotopic fluxes (He-3 and He-4) are shown in the top three panels with longitude at a fixed position, 3 au. The corresponding ratios are shown in the bottom four panels. The units for the GCR flux are $1/(m^2/sr/s/(GeV/n))$.

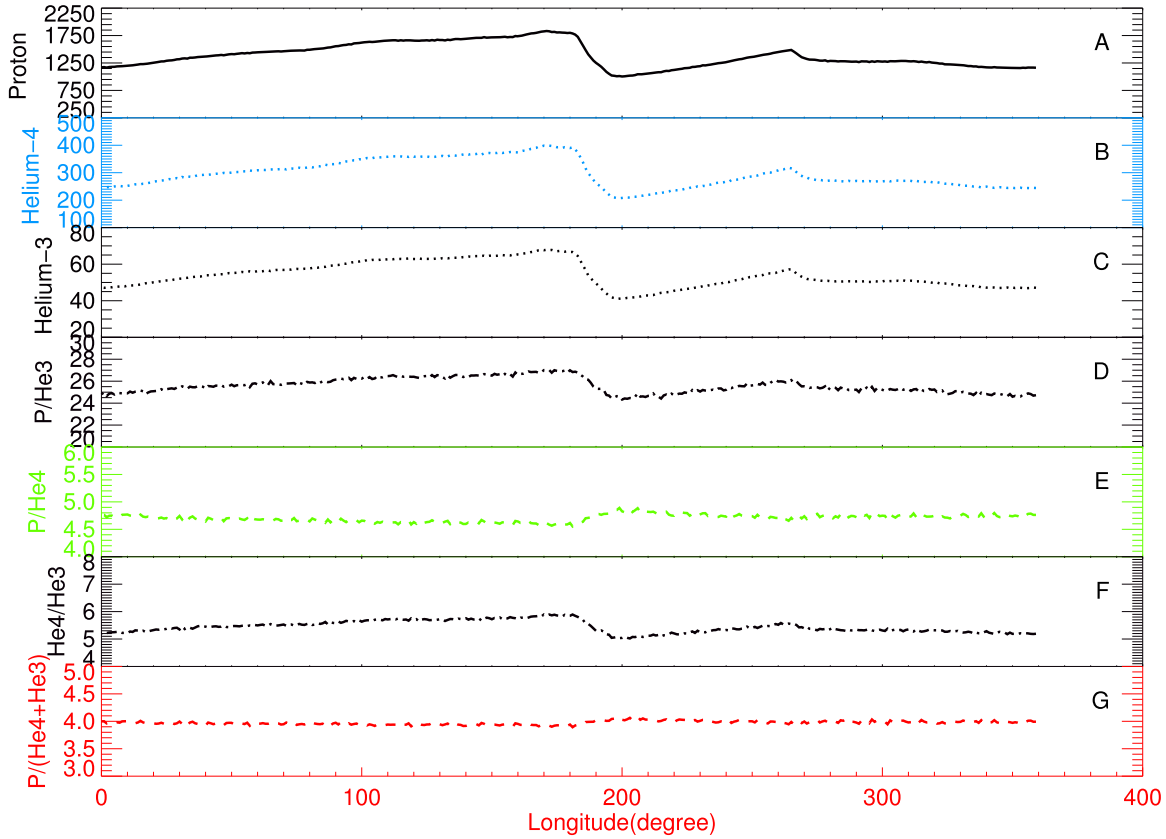

Figure 5. Similar to Figure 4, now for the simulated 1.7 GV fluxes for protons, He-3, and He-4.

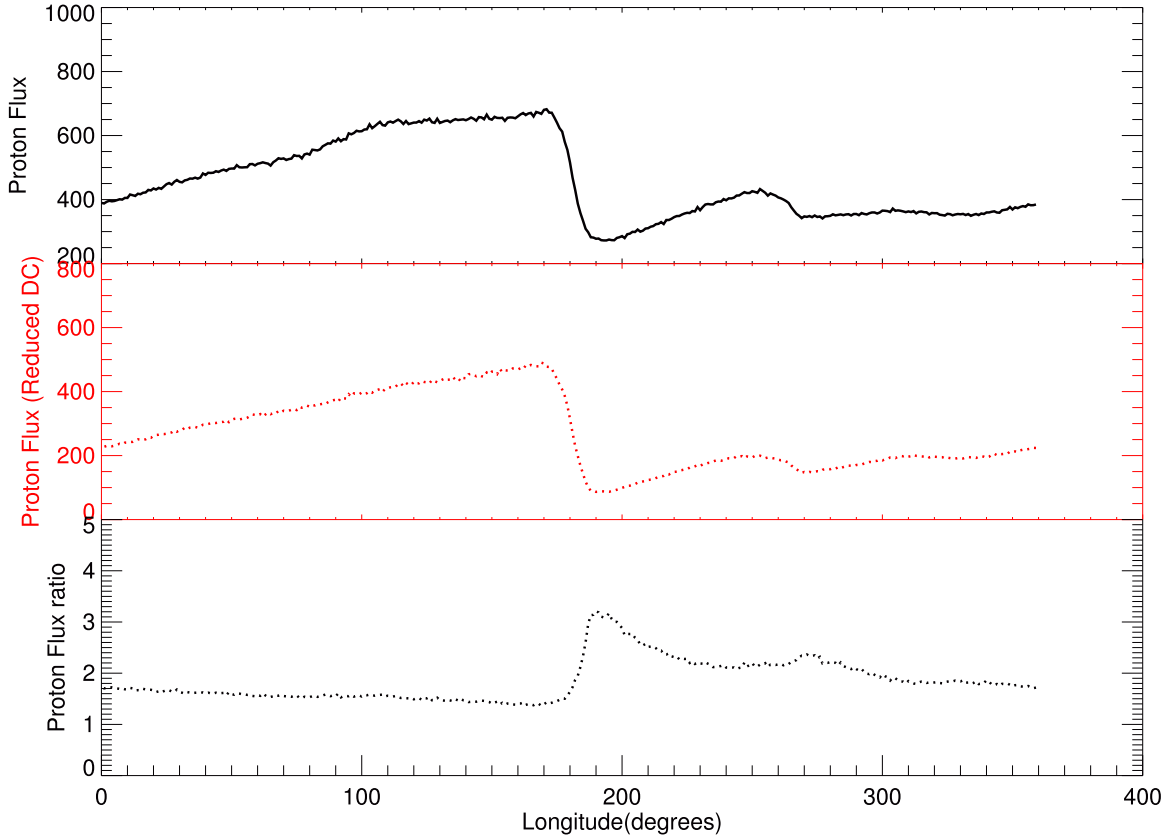

Figure 6. Simulated 0.3 GV proton-flux variation at 3 au with longitude using different DCs. The upper panel shows this with $K_0 = 17.7 \times 10^{20}$ cm^2 s^{-1}, and the middle panel shows this with $K_0' = 9.17 \times 10^{20}$ cm^2 s^{-1} in Equation (6). The units for the flux are $1/(\mathrm{m}^2/\mathrm{sr}/\mathrm{s}/(\mathrm{GeV}/\mathrm{n}))$.

In contrast, these effects on FDs are quantified (see, e.g., Luo et al. 2017, 2018; Kallaya & Yeeram 2021). However, based on a hybrid GCR transport model with a simulated CIR structure, Guo & Florinski (2014, 2016) investigated the relative roles of diffusion and drift processes. In addition to analyzing GCR and plasma observations from the ACE spacecraft, Guo et al. (2021) found that drift effects seem to rival diffusion and convection at 1 au during the recent solar minimum periods. It is not clear whether this is applicable to all rigidities.

First focusing on the diffusion process, we simulate how protons respond to the presence of a CIR using different diffusion coefficients (DCs). This is done without changing any of the other modulating parameters. Figure 6 illustrates the proton-flux variation at 0.3 GV with longitude for the changed DC value. In the upper panel, $K_0 = 17.7 \times 10^{20}$cm^2 s^{-1} in Equation 6, whereas in the middle panel, $K_0' = 9.17 \times 10^{20}$cm^2 s^{-1}, which gives $\frac{K_0}{K_0'} = 1.93$. It is noted that the ratio of the β values for protons and He-4 is also $\frac{\beta_{\mathrm{proton}}}{\beta_{\mathrm{He4}}} = 1.93$. Correspondingly, the DC for protons is reduced on the same scale as its β ratio with He-4. The lower panel shows the ratio of these two simulations for protons. It increases from 1.7 at $\phi = 0°$ to 3.3 at $\phi = 190°$, thus causing a peaked profile, indicating the role of a smaller DC in the way the CIR effects GCRs. A reduced DC thus causes a stronger effect in longitude on GCRs.

As mentioned above, it is known that for different GCR particles, even with the same rigidity, the value of β is different because it is related to the particle mass and charge. This means that for a given rigidity, the following relation exists: $\beta_{\mathrm{proton}} > \beta_{\mathrm{He3}} > \beta_{\mathrm{He4}}$. This difference progressively dissipates with increasing rigidity (see also Figure 2 by Ngobeni et al. 2020). Based on our assumptions, the DCs in Equations (6) and (7) scale proportionally to the GCR particle β value, so that the value of the DC at the same given rigidity as studied here is different for protons and He-3 and He-4: $K_{\mathrm{proton}} > K_{\mathrm{He3}} > K_{\mathrm{He4}}$. According to the argument for a reduced DC, the order of the resulting CIR effect on the maximum decrease (M) caused by the CIR is $M_{\mathrm{He4}} > M_{\mathrm{He3}} > M_{\mathrm{proton}}$. In this context, we also compare the effect of a reduced DC on a FD as studied by Luo et al. (2017). However, as shown above, the effect of the CIR on protons is stronger than on He-3, because it is different from the sequence derived from the reduced DC alone. Obviously, the difference in CIR effects for various GCR isotopes cannot solely be ascribed to a reduced DC, so that additional modulation effects, as described by PTE, should also play a role as a function of rigidity, as is found for the global modulation of GCRs (Nndanganeni & Potgieter 2016; Potgieter & Vos 2017).

The global modulation of GCRs is found to be an interplay of four distinctive processes that contribute in specific ways as a function of rigidity to the transport of GCRs (see, e.g., Potgieter & Vos 2017; Ngobeni et al. 2020, 2022). This should also be applicable to the effects of a CIR on GCRs. We thus investigate how particle drift influences the results given above. As an example, Figure 7 accordingly illustrates how the flux variation of He-4 at 0.12 GV changes with longitude when the drift coefficient is systematically reduced. We use six reduction values for $(K_d)_0$ in Equation (8). First, we simply change $(K_d)_0 = 1.0$ to $(K_d)_0 = 0.1$, which means that the selected reduction is applied over the full rigidity range, followed by

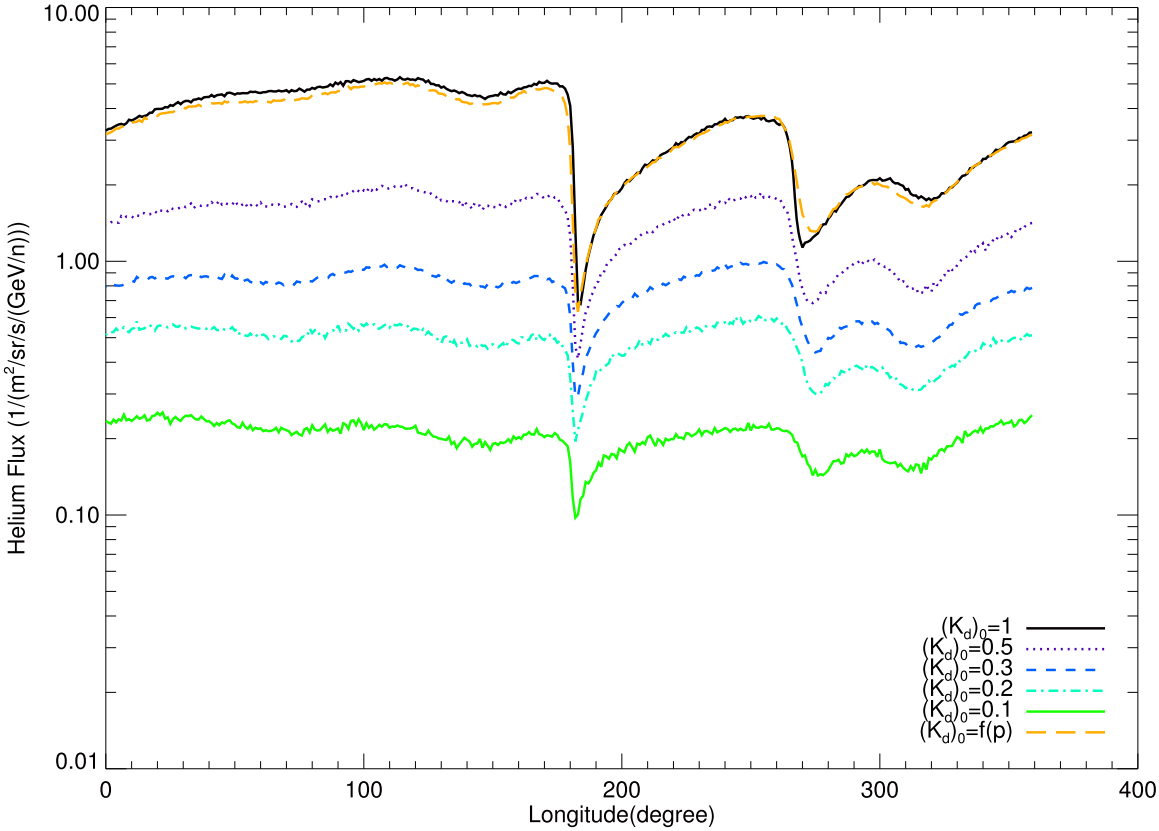

Figure 7. Simulated He-4 flux for 0.12 GV at 3 au with longitude. The colored lines represent different values for the applied drift reduction factor $(K_d)_0$ in Equation (8). The black line shows $(K_d)_0 = 1.0$; the dotted purple line shows $(K_d)_0 = 0.5$; the dashed blue line shows $(K_d)_0 = 0.3$; the dotted–dashed light green line shows $(K_d)_0 = 0.2$; the long-dashed–dotted thick green line shows $(K_d)_0 = 0.1$; and the dotted orange line shows $(K_d)_0 = 10R^2/(1 + 10R^2)$.

using $(K_d)_0 = 10R^2/(1 + 10R^2)$, which means that the reduction is applied only at lower rigidity, as is usually done in global modulation studies (e.g., Ngobeni et al. 2022; Aslam et al. 2021, 2023). These reductions are all indicated in the figure legend. It is shown here that the He-4 flux at 3 au is reduced with the scaling (reduction) of the drift coefficient, first at $\phi = 150°$, and then that the flux variation is changed with longitude. The modeled CIR is located around $\phi = [150°, 200°]$ (see Figure 3), so that the He-4 flux maximum depression value (M) caused by the CIR can be calculated with $(j_{\max} - j_{\min})/j_{\max}$, where $j_{\max}$ ($j_{\min}$) is the maximum (minimum) He-4 flux level at $\phi = [150°, 200°]$.

In Table 1 we list the quantitative variation in the M value with the applied drift reduction factor $(K_d)_0$ for the results shown in Figure 7. Obviously, it decreases considerably as drift is reduced in the numerical model. For instance, when we compare the 100% with the 10% drift, the M value changes from 0.87 to 0.55. The CIR-caused effects are thus affected by how small the assumed drift coefficient is. In other words, it demonstrates the influence of the drift process on the extent of the effects of a CIR on GCRs. It is noted that in Figure 7, there is little difference between $(K_d)_0 = 1.0$ (black curve), and $(K_d)_0 = 10R^2/(1 + 10R^2)$ (orange curve). Because cosmic-ray transport in the heliosphere includes an energy-loss process, the rigidity ranges from the selected value ($R = 0.12$ GV) to high values ($R > 1$ GV). The simulation indicates that the reduction of the particle drift at lower rigidity ($R < 1$ GV) alone does not cause a significant effect at this selected rigidity value.

Table 1
GCR Depression Value Used for Figure 7

Drift Reduction Factor	CIR-introduced Depression Value
$(K_d)_0 = 1.0$	0.87
$(K_d)_0 = 0.5$	0.78
$(K_d)_0 = 0.3$	0.69
$(K_d)_0 = 0.2$	0.64
$(K_d)_0 = 0.1$	0.55
$(K_d)_0 = 10R^2/(1 + 10R^2)$	0.86

3.3. Rigidity Dependence of CIR Effects

The rigidity dependence of the CIR-induced GCR variation has been explored before both experimentally and theoretically. Based on observational data in 1992–93 from the Ulysses spacecraft, Paizis et al. (1999) reported the rigidity dependence of the GCR variations (for both protons and He) and found evidence with limited data points that a maximum effect occurred at about several hundred megavolts. They also reported a remarkable similarity between the rigidity dependence of the GCR latitudinal variation and that of the 27 day variation (see also Zhang 1997). Analyzing neutron monitor data, Gil & Alania (2016) calculated the rigidity dependence of the GCR recurrent variations for different solar cycle phases and established that it clearly varied with solar activity. Leske et al. (2011, 2019) also studied this effect using ACE measurements, along with neutron monitor data, during the last two solar minima. Recently, based on the observational data from PAMELA and ARINA, Modzelewska et al. (2020)

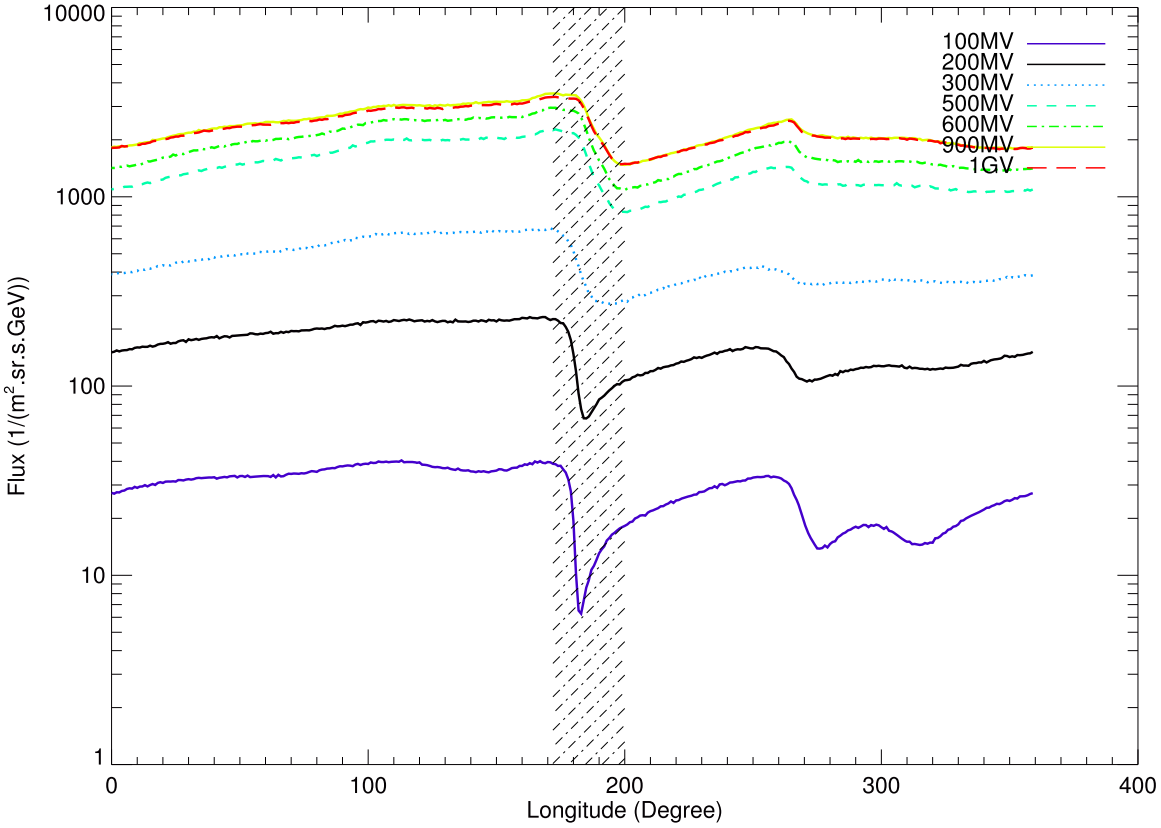

Figure 8. Simulated proton-flux variation at 3 au caused by a CIR as a function of longitude for seven rigidity levels, as indicated by different colors. As in Figure 3, the CIR is located at this distance at around a longitude of 180°, indicated as the shaded area.

presented the rigidity dependence of the amplitude of the GCR proton 27 day variation between ∼0.3 and ∼10 GV. They found that this rigidity dependence cannot be fit with a single power law. Instead, the power-law shape levels off at ∼1 GV, and additionally, a local maximum exists in this dependence at ∼0.6 GV (see their Figures 7 and 8). With precise measurements of the GCR flux from AMS, in terms of a high time and rigidity resolution, Aguilar et al. (2021, 2022) reported the GCR recurrent variation with different timescales (27 days, 13.5 days, and 9 days) and that the strength of the different recurrent periodicity varies with time and rigidity. The AMS data also reveal that the rigidity dependence of the strength of these recurrent periodicity does not follow a simple trend.

In Part I, the rigidity dependence was investigated by simulating the GCR proton-flux variation inside the CIR for seven energy levels. The results were used to calculate the GCR variation amplitude. Although the study reveals a weak (flat) energy dependence of the amplitude at around 100 MeV for protons, there is no information about the rigidity dependence of the CIR effect in the lower-energy range (∼0.2 GV). The overall rigidity dependence is still being obscured. Ironically, some decades ago, Paizis et al. (1999) stated that there was no numerical study for the rigidity dependence of these 27 day variations. As far as we can determine, numerical studies of this rigidity dependence have indeed been absent. Here, based on our hybrid model, we have extended the previous study to a lower rigidity, striving to establish a more complete picture of the rigidity dependence of the mentioned amplitude.

Figure 8 illustrates the simulated GCR proton-flux variation due to the presence of a CIR with longitude at 3 au for seven rigidity levels. Similarly, the He-4 flux variation is illustrated in Figure 9. Evidently, the flux depression level for the GCRs decreases the higher the rigidity, as shown within the shaded region. The other variations in longitude are also stronger at the lower rigidity. The shape of the flux depression in longitude is also smoother at high rigidity and becomes progressively better defined at and below 200 MV. This occurs because these low-rigidity GCRs with their smaller gyroradii sense the induced changes in the magnetic field on a smaller scale.

Adopting an established expression for the amplitude of the maximum decrease (depression), $A = ((j_{\max} - j_{\min})/j_{\max})$, it is calculated for each individual GCR proton and He depression (as indicated by the shaded regions in the previous figures) as a function of rigidity from 0.1 GV up to ∼10 GV. Figure 10 shows the obtained amplitude variation with rigidity for protons, and Figure 11 shows the case for He-4.

Investigating and focusing on the decreasing trend for $R >$ 1 GV, we found that it can be fit by a power-law function with $A \propto R^{\gamma}$; with $\gamma = -0.438$ for protons, and $\gamma = -0.47$ for He-4. This is displayed in Figures 10 and 11, respectively. In our transport model, we assumed that all the diffusion coefficients scale proportionally to a prescribed function of the rigidity, as shown in Equations (6) and (7), with a power index of 0.47 at $R \gtrsim R_k$. This value relates markedly well to what is shown in these two figures. This equality relation provides straightforward evidence of the extent to which diffusion plays a role for CIR-induced GCR variations. It is interesting to note that this provides an alternative (perhaps even an additional) approach of determining the rigidity dependence of the DCs in numerical models using observational CIR data. Furthermore, it may

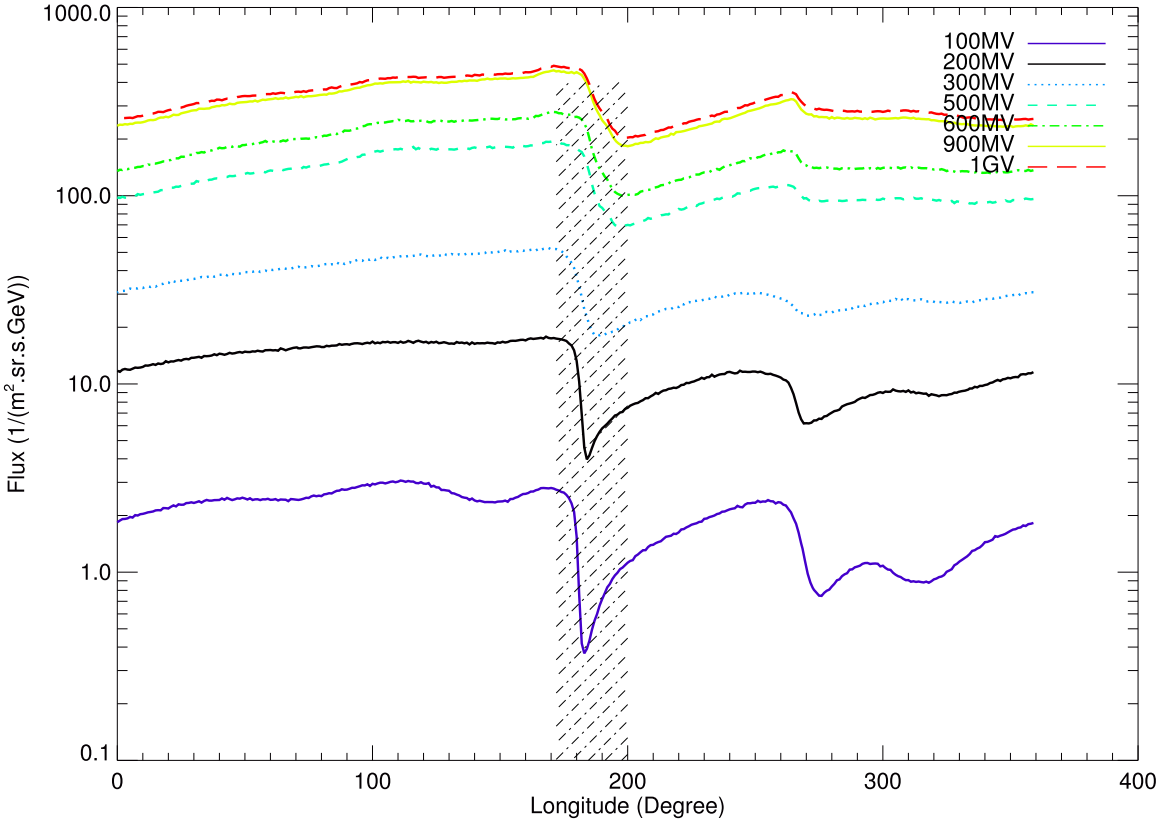

Figure 9. Similar to Figure 8, now for He-4 fluxes.

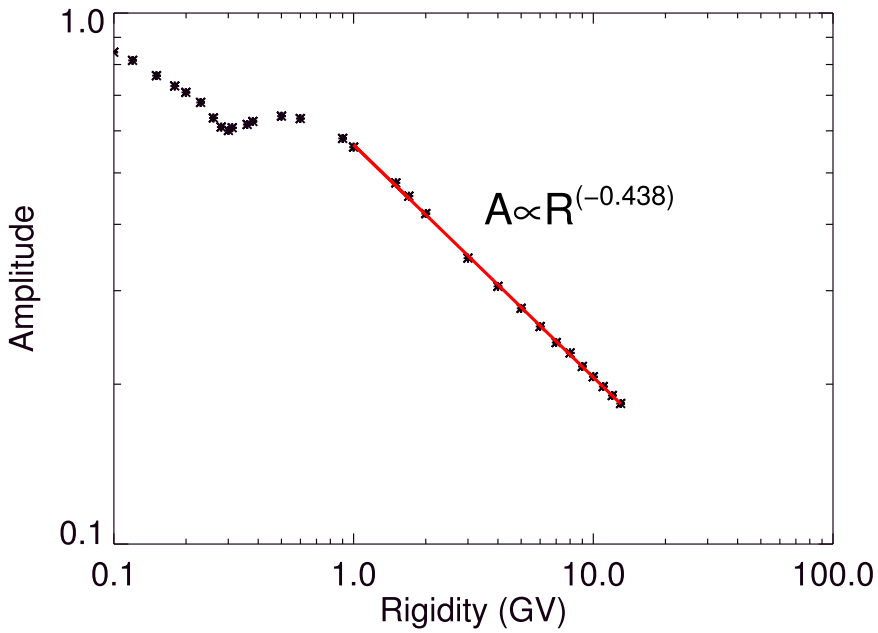

Figure 10. Rigidity dependence (R) of the amplitude (A) of the maximum decrease in the proton-flux variations induced by the CIR. The decreasing trend for $R > 1$ GV is fit by a power-law function with $A \propto R^{-0.438}$.

indicate how the DCs change with solar activity over this rigidity range.

Focusing on lower rigidity, between 0.3 and 0.8 GV, both Figures 10 and 11 display a flattening (plateau-like) trend with a clear and prominent local peak at ∼0.5 GV for protons, but a somewhat weaker peak for He-4. At an even lower rigidity (<0.3 GV), after displaying a clear local minimum, the amplitude again increases systematically with decreasing rigidity, with some indication of a change (decrease) in the slope at the lowest rigidity shown here. The overall trends, as well as the local peak, seem consistent with what Modzelewska et al. (2020) reported for protons. Qualitatively, these simulations reveal that for the lower rigidity range, the amplitude increases significantly with decreasing rigidity. It

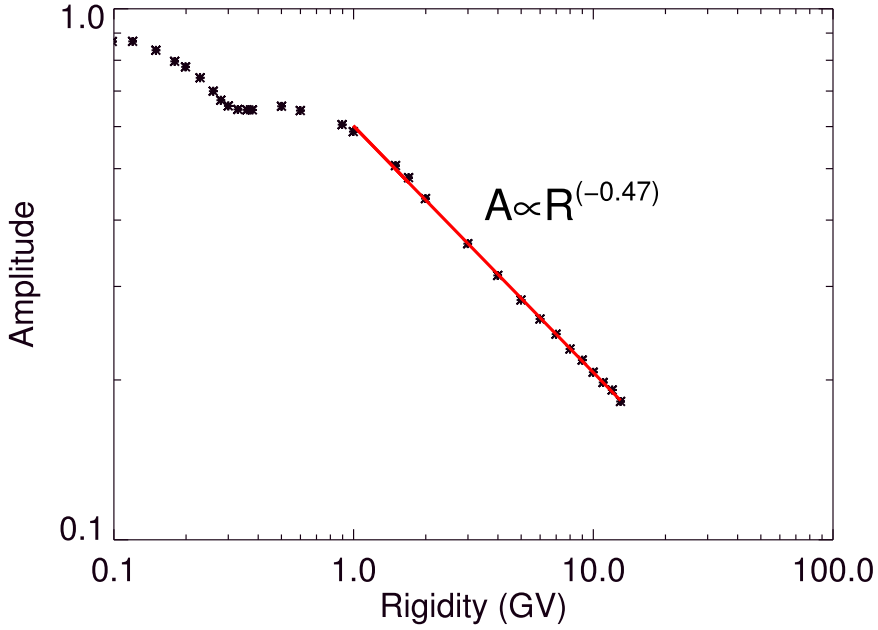

Figure 11. Similar to Figure 10, here for He-4.

should be noted that we calculate the amplitude differently from what Modzelewska et al. (2020) assumed to analyze the amplitude of the 27-day GCR variations, so that the values differ quantitatively.

It is shown in Figure 2 that the rigidity slopes of the DCs change significantly with decreasing rigidity between 4 and 1 GV, eventually steadying below about 500 MV into a different power law with a power index significantly higher than 4 GV. The amplitude-rigidity dependence displayed in Figures 10 and 11 shows a strong change between 0.8 and 0.3 GV that deviates significantly from the power-law shape at higher rigidity, but then, with further decreasing rigidity, picks up another power-law shape below 300–400 MV. This power law, however, does not match the power-law index of the DCs as found for the high rigidity. This indicates that the GCR modulation at lower rigidity becomes more complicated, which is a manifestation of the interplay between diffusion, drift, and adiabatic energy losses, which dominates at lower rigidity $R < \sim 300$ MV and is therefore less easy to disentangle. The amplitude-rigidity dependence is therefore no longer straightforward to interpret. We refer to Figures 6 and 7 from Potgieter & Vos (2017) for an illustration at which the rigidity range drift effects are strongest and how they weaken to subside for adiabatic energy losses to become dominant. In this context, see also Ngobeni et al. (2020, 2022) for simulated proton, He-3, and He-4 spectra at the Earth and how their respective very LISs affect them.

We consider a simulation study of how the amplitude may vary with the solar cycle (time) as a function of rigidity as a future project (see the report of these aspects by Heber et al. 1999 based on Ulysses observations). Similarly seen is the fine-tuning of simulations in order to obtain results that may be directly compared with observations. In addition, with new AMS observations of the CIR effects over an extended period of time, it may become possible to investigate charge-sign-dependent effects in CIRs as conclusive evidence of the influence of particle drift. It should be noted that using MHD simulations together with an SDE approach to GCR modulation does not make the investigation of the latter aspects an easily done task.

4. Summary, Conclusions, and Outlook

In this study, an MHD model is adopted to simulate the background solar wind plasma up to ∼27 au. By extrapolating the inner MHD-simulated plasma with a Parker magnetic field model, a whole simulation domain is constructed. The CIR structure in the inner MHD-simulated heliosphere is incorporated into the SDE transport model to study CIR effects on GCR transport, especially in terms of their distribution in heliolongitude. The focus is on the simulation of these effects for GCR protons and the two helium isotopes to establish whether the difference in composition affects how they are modulated by the CIR.

Simulations of the proton and helium isotopic fluxes (He-4 and He-3) associated with the CIR indicate when calculating the flux ratios that protons and helium isotopes are modulated differently with longitude by the CIR, but that these differences dissipate with increasing rigidity to become negligible for the higher-rigidity regime. This difference, however, is not of a fundamental nature, but is related to the difference between these GCR particles in terms of their charge-to-mass ratio (and the corresponding β-dependence on the DCs) and their respective very LISs. It is also demonstrated that particle diffusion and drift influence the effects of the CIR on GCRs in longitude and with rigidity, ranging between 100 MV and 15 GV.

The final simulations are focused on the amplitude of the CIR-caused variation for protons and He-4 as a function of rigidity. It is found that the amplitude of the CIR-caused variation for protons and He-4 display a power-law behavior above ∼1 GV with an index similar to the power index of the diffusion coefficients. This indicates that the diffusion process plays a determining role in establishing the rigidity dependence of the amplitude at high rigidity. It thus follows that the rigidity dependence of this amplitude contains information about the

rigidity dependence of the DCs, again related to the charge-to-mass ratio of the GCRs.

However, between 0.3 and 0.8 GV, the simulated amplitude-rigidity profile exhibits a plateau-like trend with a local peak at ∼0.5 GV. Similar trends were reported by Paizis et al. (1999) and Modzelewska et al. (2020), and it is qualitatively consistent with our previous study (Luo et al. 2020). As for the lower rigidity, $R < 0.3$ GV, the amplitude again changes to increase systematically with decreasing rigidity, displaying yet another power-law shape, but with a power index completely different from that of the DCs. Our interpretations is that at these rigidities, the effects of the CIR on GCR transport are the consequence of the interplay (entanglement) of the modulation processes, namely, diffusion, drift, and adiabatic energy losses. In the inner heliosphere, the latter dominates in determining the spectral shape of these GCRs at $R < \sim 300$ MV, as is consistently found for the global modulation of GCRs.

Recently, the AMS collaboration reported the rigidity dependence of recurrent flux variations for GCR protons and He up to ∼100 GV (Aguilar et al. 2021, 2022) over an extended period of time. This now also includes precise electron observations (Aguilar et al. 2023), so that the assumed charge-sign dependence of CIR-caused GCR variations could be properly investigated. It is reasonable to conclude that these precise observations together with distinctive numerical models may contribute to unraveling the reported mystery and associated confusion about the CIR phenomenon in GCR modulation in the near future.

Acknowledgments

The present work is jointly supported by the startup funding of the Shandong Institute of Advanced Technology No. 2020106R01, Taishan Scholar Project of Shandong Province No. 202103143, and NSFC grants No. U2106201 and No. 42150105. F.S. is supported by National Key RD Program of China (Grant Nos. 2022YFF0503800 and 2021YFA0718600). We are grateful for discussions with Professors Xueshang Feng, Galina Bazilevskaya, Mikhail Krainev, and Weiwei Xu.

ORCID iDs

Xi Luo https://orcid.org/0000-0002-4508-6042
Marius S. Potgieter https://orcid.org/0000-0003-0793-7333
Ming Zhang https://orcid.org/0000-0003-3529-8743
Fang Shen https://orcid.org/0000-0002-4935-6679

References

Adriani, O., Barbarino, G. C., Bazilevskaya, G. A., et al. 2013, ApJ, 765, 91
Aguilar, M., Cavasonza, L., Ambrosi, G., et al. 2021, PhRvL, 127, 271002
Aguilar, M., Cavasonza, L., Ambrosi, G., et al. 2022, PhRvL, 128, 231102
Aguilar, M., Cavasonza, L., Ambrosi, G., et al. 2023, PhRvL, 130, 161001
Aguilar, M., Cavasonza, L. A., Ambrosi, G., et al. 2021, PhRvL, 127, 271102
Aslam, O. P. M., Bisschoff, D., Ngobeni, M. D., et al. 2021, ApJ, 909, 215
Aslam, O. P. M., Luo, X., Potgieter, M. S., et al. 2023, ApJ, 947, 72
Bisschoff, D., Potgieter, M. S., & Aslam, O. P. M. 2019, ApJ, 878, 59
de Simone, N., di Felice, V., Gieseler, J., et al. 2011, ASTRA, 7, 425
Decker, R. B., Krimigis, S. M., Ananth, A. G., Hamilton, D. C., & Hill, M. E. 1999, ICRC (Salt Lake City, UT), 7, 512
Dumbović, M., Vršnak, B., Temmer, M., Heber, B., & Kühl, P. 2022, A&A, 658, A187
Dunzlaff, P., Heber, B., Kopp, A., et al. 2008, AnGeo, 26, 3127
Engelbrecht, N. E., Strauss, R. D., le Roux, J. A., et al. 2017, ApJ, 841, 107
Forman, M. A., Jokipii, J. R., & Owens, A. J. 1974, ApJ, 192, 535
Gazis, P. R., McDonald, F. B., Burger, R. A., et al. 1999, SSRv, 89, 269
Ghanbar, K., & Florinski, V. J. 2023, ApJ, 943, 87
Gieseler, J., & Heber, B. 2016, A&A, 589, A32
Gil, A., & Alania, M. V. 2016, SoPh, 291, 1877
Guo, X., & Florinski, V. 2014, JGRA, 119, 2411
Guo, X., & Florinski, V. 2016, ApJ, 826, 65
Guo, X., Florinski, V., Wang, C., & Ghanbari, K. 2021, ApJ, 910, 99
Heber, B., Sanderson, T. R., & Zhang, M. 1999, AdSpR, 23, 567
Jokipii, J. R., & Kóta, J. 1995, SSRv, 72, 379
Jokipii, J. R., Levy, E. H., & Hubbard, W. B. 1977, ApJ, 213, 861
Kallaya, O., & Yeeram, T. 2021, Ap&SS, 366, 61
Kopp, A., Wiengarten, T., Fichtner, H., et al. 2017, ApJ, 837, 37
Kóta, J., & Jokipii, J. R. 1983, ApJ, 265, 573
Kóta, J., & Jokipii, J. R. 1991, GeoRL, 18, 1797
Krainev, M., Kalinin, M., Bazilevskaya, G., et al. 2023, STP, 9, 9
Kunow, H., Dröge, W., Heber, B., et al. 1995, SSRv, 72, 397
Kunow, H., Lee, M. A., Fisk, L. A., et al. 1999, SSRv, 89, 221
Leske, R., Cummings, A. C., Mewaldt, R. A., et al. 2011, ICRC (Beijing), 11, 194
Leske, R., Cummings, A. C., Mewaldt, R. A., et al. 2019, ICRC (Madison, WI), 36, 1105
Luo, X., Potgieter, M. S., Zhang, M., et al. 2016, ApJ, 826, 182
Luo, X., Potgieter, M. S., Zhang, M., & Feng, X. 2017, ApJ, 839, 53
Luo, X., Potgieter, M. S., Zhang, M., & Feng, X. 2018, ApJ, 860, 160
Luo, X., Zhang, M., Feng, X., et al. 2020, ApJ, 899, 90
Luo, X., Zhang, M., Potgieter, M. S., & Pogorelov, N. V. 2015, ApJ, 808, 82
Luo, X., Zhang, M., Rassoul, H. K., et al. 2011, ApJ, 730, 13
Luo, X., Zhang, M., Rassoul, H. K., et al. 2013, ApJ, 764, 85
Marcelli, N., Boezio, M., Lenni, A., et al. 2020, ApJ, 893, 145
Martucci, M., Munini, R., Boezio, M., et al. 2018, ApJL, 854, L2
McKibben, R. B., Jokipii, J. R., Burger, R. A., et al. 1999, SSRv, 89, 307
Modzelewska, R., Bazilevskaya, G. A., Boezio, M., et al. 2020, ApJ, 904, 3
Ngobeni, M. D., Aslam, O. P. M., Bisschoff, D., et al. 2020, Ap&SS, 365, 182
Ngobeni, M. D., & Potgieter, M. S. 2015, AdSpR, 56, 1525
Ngobeni, M. D., Potgieter, M. S., & Aslam, O. P. M. 2022, AdSpR, 69, 2330
Ndanganeni, R. R., & Potgieter, M. S. 2016, AdSpR, 58, 453
Odstrcil, D. 2003, AdSpR, 32, 497
Paizis, C., Heber, B., Ferrando, P., et al. 1999, JGR, 104, 28241
Parker, E. N. 1965, P&SS, 13, 9
Pizzo, V. J. 1982, JGR, 87, 4374
Potgieter, M. S., & Moraal, H. 1985, ApJ, 294, 425
Potgieter, M. S., & Vos, E. 2017, A&A, 601, A23
Potgieter, M. S., Vos, E. E., Boezio, M., et al. 2014, SoPh, 289, 391
Richardson, I. G. 2004, SSRv, 111, 267
Richardson, I. G. 2018, LRSP, 15, 1
Richardson, I. G., Wibberenz, G., & Cane, H. V. 1996, JGR, 101, 13483
Shen, F., Yang, Z., Zhang, J., Wei, W., & Feng, X. 2018, ApJ, 866, 18
Shen, Z. N., Qin, G., Zuo, P., Wei, F., & Xu, X. 2021, ApJ, 256, 18
Shiota, D., Zank, G. P., Adhikari, L., et al. 2017, ApJ, 837, 75
Song, X., Luo, X., Potgieter, M. S., Liu, X., & Geng, Z. 2021, ApJS, 257, 48
Usmanov, A., Matthaeus, W. H., Goldstein, M. L., & Chhiber, R. 2018, ApJ, 865, 25
Vos, E. E., & Potgieter, M. S. 2016, SoPh, 291, 181
Wiengarten, T., Kleimann, J., Fichtner, H., et al. 2014, ApJ, 788, 80
Yang, Z., Fang, S., Yi, Y., & XueShang, F. 2018, ChJG, 61, 4337
Zhang, M. 1997, ApJ, 488, 841
Zhang, M. 1999, ApJ, 513, 409
Zhao, L.-L., Adhikari, L., Zank, G. P., Hu, Q., & Feng, X. S. 2017, ApJ, 849, 88
Zhao, L.-L., Adhikari, L., Zank, G. P., Hu, Q., & Feng, X. S. 2018, ApJ, 856, 94